NeuroImage 106 (2015) 328–339

Contents lists available at ScienceDirect

NeuroImage

journal homepage: www.elsevier.com/locate/ynimg

Role of white-matter pathways in coordinating alpha oscillations in resting visual cortex

R. Hindriks [a,*], M. Woolrich [b], H. Luckhoo [b,e], M. Joensson [c,d], H. Mohseni [b], M.L. Kringelbach [c,d], G. Deco [a,f]

[a] Center for Brain and Cognition, Computational Neuroscience Group, Department of Information and Communication Technologies, Universitat Pompeu Fabra, Roc Boronat 138, Barcelona 08018, Spain
[b] Oxford Centre for Human Brain Activity, University of Oxford, Warneford Hospital, Oxford OX37JX, UK
[c] Department of Psychiatry, University of Oxford, Warneford Hospital, Oxford OX37JX, UK
[d] Center of Functionally Integrative Neuroscience (CFIN), Aarhus University, Denmark
[e] Centre for Doctoral Training in Healthcare Innovation, Institute of Biomedical Engineering, Department of Engineering Science, University of Oxford, UK
[f] Instituci Catalana de la Recerca i Estudis Avanats (ICREA), Universitat Pompeu Fabra, Passeig Llus Companys 23, Barcelona, 08010, Spain

ARTICLE INFO

Article history:
Accepted 26 October 2014
Available online 30 October 2014

ABSTRACT

In the absence of cognitive tasks and external stimuli, strong rhythmic fluctuations with a frequency ≈10 Hz emerge from posterior regions of human neocortex. These *posterior α-oscillations* can be recorded throughout the visual cortex and are particularly strong in the calcarine sulcus, where the primary visual cortex is located. The mechanisms and anatomical pathways through which local \alpha-oscillations are coordinated however, are not fully understood. In this study, we used a combination of magnetoencephalography (MEG), diffusion tensor imaging (DTI), and biophysical modeling to assess the role of white-matter pathways in coordinating cortical α-oscillations. Our findings suggest that primary visual cortex plays a special role in coordinating α-oscillations in higher-order visual regions. Specifically, the amplitudes of α-sources throughout visual cortex could be explained by propagation of α-oscillations from primary visual cortex through white-matter pathways. In particular, α-amplitudes within visual cortex correlated with both the anatomical and functional connection strengths to primary visual cortex. These findings reinforce the notion of posterior α-oscillations as intrinsic oscillations of the visual system. We speculate that they might reflect a default-mode of the visual system during which higher-order visual regions are rhythmically primed for expected visual stimuli by α-oscillations in primary visual cortex.

Introduction

The most salient feature of electrical activity in human neocortex in the absence of explicit cognitive tasks is strong ≈10 Hz oscillations (Berger, 1875; Hari and Salmelin, 1997). These posterior α-oscillations are typically recorded over occipital and posterior-parietal regions and are particularly strong within and around the calcarine fissure—where the primary visual cortex (V1) is located—as well as in the occipito-parietal fissure (Hari and Salmelin, 1997; Ciulla et al., 1999). Although initially regarded as functionally irrelevant, evidence is now accumulating that posterior α-oscillations do not merely reflect passive idling of visual areas but correlate with allocation of visuo-spatial attention (Yamagishi et al., 2005; Jensen et al., 2010; Capilla et al., 2012). For example, during anticipatory cue-stimulus intervals, α decreases in those regions of V1 that correspond to attended locations in the visual field and increases in unattended or distractor regions (Kelly et al., 2006; Rihs et al., 2007). Moreover, these modulations do not only pertain to spatial attention tasks but extend to feature-based attentional processes in higher-order visual areas including the dorsal and ventral projection systems (Jokisch and Jensen, 2007; Snyder and Foxe, 2010). Thus, power fluctuations in posterior α-oscillations seem to reflect modulations in cortical excitability, constituting a fundamental mechanism for flexible routing of visual attention (Jensen et al., 2002; Romei et al., 2008; Spaak et al., 2012). Research on the neuronal mechanisms underlying attention-driven α-modulation is expected to benefit from a characterization of the resting-state organization of posterior α-oscillations.

Magnetoencephalographic (MEG) recordings in human subjects and local field potential (LFP) recordings in dogs and macaques have shown that posterior α-oscillations can be recorded throughout the visual system (Lopes Da Silva and Storm van Leeuwen, 1977; Salmelin and Hari, 1994; Hari and Salmelin, 1997; Ciulla et al., 1999; Bollimunta et al., 2008, 2011; Spaak et al., 2012). In addition to cortical sources of α, recordings in behaving dogs and slice preparations of cat lateral geniculate nucleus (LGN) have observed α-sources in thalamic nuclei, particularly the LGN and pulvinar (Lopes da Silva et al., 1973; Hughes et al., 2004). Moreover, the time-courses of sources in LGN and in particular the pulvinar were correlated with various α-sources in occipital cortex (Lopes Da Silva et al., 1980). Furthermore, EEG-fMRI recordings in humans have found resting-state fluctuations in posterior α-power

* Corresponding author.
E-mail address: Rikkert.Hindriks@upf.edu (R. Hindriks).

http://dx.doi.org/10.1016/j.neuroimage.2014.10.057
1053-8119/

to be correlated with fluctuations in blood-level-oxygenation-level (BOLD) signal throughout the visual system and in several subcortical nuclei (Goldman et al., 2002; Moosmann et al., 2003; Feige et al., 2005). Thus, although posterior α-oscillations seem to involve large-scale thalamo-cortical networks, the nature of their involvement remains controversial (Silva et al., 1991; Karameh et al., 2006).

In particular, it is unclear if α-oscillations are generated at the source locations identified by MEG or if they are generated at other locations and propagate through white-matter pathways. For example, α-oscillations in V1 might be generated within V1 itself (Liley et al., 1999), reflect propagated oscillations that are generated in the LGN (Lopes da Silva et al., 1974; Hughes et al., 2004), which is densely connected to V1 via the optic radiation, or reflect reverberation within thalamo-cortical loops (Robinson et al., 2001; Rennie et al., 2002). Similarly, α-oscillations in different regions of the visual system might be generated locally or reflect propagated oscillations from distant cortical or thalamic regions. In this study, we assessed the contribution of white-matter pathways in the propagation and coordination of posterior α-oscillations. To this end, we combined MEG source-modeling (Woolrich et al., 2011), diffusion tensor imaging (DTI) based probabilistic fiber tracking (Behrens et al., 2003b), and biophysical modeling.

The kind of biophysical model we used in this study is referred to as a *neural mass model*. Neural mass models have a long tradition (Wilson and Cowan, 1973; Lopes da Silva et al., 1974; Freeman, 2004) and have been applied to several EEG phenomena, including \alpha-oscillations (Lopes da Silva et al., 1974), event-related potentials (Jansen and Rit, 1995), and epileptic seizures (Suffczynski et al., 2004). Neural mass models describe the electrical behavior of a piece of neural tissue in terms of macroscopic quantities and ignore the spatial extendedness of the tissue (Deco et al., 2008). An extension of neural mass models are so-called *neural field models* which can be thought of as consisting of a sheet of neural masses and describe the electrical behavior of neocortex in a spatially continuous manner (Deco et al., 2008). Neural fields have a long tradition as well (Wilson and Cowan, 1973; Nunez, 1974; Wright and Liley, 1995) and also have been applied to several EEG phenomena including delta, alpha, beta, and gamma oscillations (Nunez et al., 2001; Liley and Cadusch, 2002; Rennie et al., 2000, 2002; Robinson et al., 2001), sleep (Robinson et al., 2002; Steyn-Ross et al., 2005), and general anesthesia (Bojak and Liley, 2005; Hutt and Longtin, 2010; Hindriks and van Putten, 2012). They provide a theoretical framework in which different EEG phenomena can be integrated and their relationships be investigated (Robinson et al., 2001; Breakspear et al., 2006).

The motivation for using a neural mass model in the present study is that they make more feasible an initial investigation into how posterior \alpha-oscillations might emerge from the topology of white-matter pathways and provide a direction for more extented modeling studies. It is of interest to note though, that the combination of neural mass models with white-matter topological data has proven effective in modeling the emergence of resting-state networks (RSNs) in blood-oxygenation level-depend(BOLD) functional magnetic resonance imaging (fMRI) imaging (Ghosh et al., 2008; Deco et al., 2009, 2011, 2013; Honey et al., 2009; Cabral et al., 2011). Thus, the current study should be regarded as an initial orientation that provides a startingpoint for constructing more extended models of the spatio-temporal behavior of \alpha-oscillations in human cortex.

We found that the assumption of a single α-source in the calcarine sulcus (V1) could explain the source-strengths of α-oscillations throughout the occipital lobe, medial posterior–parietal cortex and temporal lobes. Furthermore, the source-strengths of α-oscillations in these regions correlated with both the functional and anatomical connections to V1, consistent with the assumption of a generator in V1. Although this study does not rule out the possibility that α-oscillations are generated throughout the cortex (Robinson et al., 2001; Rennie et al., 2002; Nunez and Srinivasan, 2006), it establishes a central role of V1-connectivity in coordinating α-oscillations in the visual system at rest.

Materials and methods

MEG recordings

Ten subjects (3 males, 20–39 years old, mean 27.9) underwent an eyes-closed resting-state MEG scan lasting 5 min on an Elekta Neuromag (Elekta Neuromag Oy, Helsinki, Finland). Data preprocessing included signal space separation, de-noising with independent component analysis (ICA), source reconstruction and bandpass filtering of the MEG signal. External noise was removed using Signal-Space Separation (SSS) and the data was down-sampled to 200 Hz, using the MaxFilter software (Elekta-Neuromag). Signal space separation is a spatial filtering applied to the sensor space data that compensates for external interference and sensor artifacts. This works by projecting the MEG data onto a basis set of spherical harmonics, followed by the removal of the basis functions that correspond to sources originating from outside the sensor array, before reconstructing the data (Taula et al., 2005). Harmonics corresponding to sources originating from within the sensor array were preserved whilst interfering sources from outside the environment surrounding the sensor array were rejected. The sensor-space MEG data were de-noised using temporal ICA to remove cardiac, 50 Hz mains and, in some subjects, eye movement artifacts.

Specifically, the data were decomposed into 64 components using fastICA (Hyvarinen, 1999) (64 is the rank of the MEG data after signal space separation). Prior to the ICA decomposition, each sensor type was normalized by its smallest eigenvalue to give an unbiased noise estimate across sensor types. Eye-blink, cardiac and mains interference ICA components were manually identified by the combined inspection of spatial topography and time course, kurtosis of the time course, and frequency spectrum for all components. The artifact components are removed by subtracting them from the data (Mantini et al., 2011). This enabled simultaneous de-noising of the data and correction of the lead fields (via the montage function in SPM8).

Each dataset was then co-registered into the Montreal Neurological Institute (MNI) space by registering the canonical MNI template to the Polhemus head shape data. A local sphere forward model (Huang et al., 1999) was then estimated using the head shape and sensor geometry. Before acquisition of the MEG data, a three-dimensional digitizer (Polhemus Fastrack) was used to record each subject's head shape relative to the position of the head position indicator (HPI) coils, with respect to three anatomical landmarks, or fiducials, which could be registered on the MRI scan (the nasion, and the left and right preauricular points). A structural MRI was also acquired. Individual meshes (including scalp, inner skull and cortical surfaces) are generated from an individual subjects structural MRI by applying the inverse of the same deformation field needed to normalize the individual structural image to an MNI template, to the canonical meshes derived from the MNI template (Mattout et al., 2007). Coregistration of the MEG sensor positions with the structural MRI and the meshes is then carried out via an approximate matching of the fiducials in the two spaces, followed by a more accurate surface-matching routine that fits the head-shape function (measured by Polhemus) to the scalp mesh. This procedure was carried out using scripts in the SPM8 package. Lead fields were computed using a single-shell head model (Nolte, 2003) based on the inner skull mesh using scripts in the SPM8 package.

Subsequently, the MEG data were bandpass filtered between 1 and 80 Hz. A LCMV beamformer was used to transform the original sensor time-series into source-space time-series, that is, to reconstruct the activity at the 90 center locations defined by the AAL brain parcellation. The beamformer uses the forward model and sensor-space covariance matrix to calculate a set of weights which spatially filter the signal so that activity from outside the source is suppressed and the activity from the chosen sources is extracted (Woolrich et al., 2011). The magnetometers and gradiometers were combined during beamforming by normalizing the data and lead fields for each sensor type by its respective minimum eigenvalue; this effectively gives both classes of sensor

equal noise levels. We discarded the reconstructed time-series of all subcortical regions because their lower reliability and subsequently filtered the remaining time-series in the α frequency band (7 − 13) Hz and computed their standard-deviations. This resulted in source-strength estimates for all cortical AAL regions, which are shown in Fig. 1A.

Diffusion tensor imaging

Diffusion tensor imaging (DTI) data were acquired for 21 healthy participants (10 females, age range 22–45 years) on a Philips Achieva 1.5 Tesla Magnet in Oxford. Diffusion weighted imaging was performed using a single-shot echo planar sequence with coverage of the whole brain. DTI data were acquired with 33 optimal nonlinear diffusion gradient directions (b = 1200 s/mm2) and 1 non-diffusion weighted volume (b = 0). The scanning parameters were echo time (TE) = 65 ms and repetition time (TR) = 9390 ms. For 9 of the 21 participants the reconstructed matrix size was 176 × 176 with voxel size of 1.8 × 1.8 × 2.0 mm, while the remaining 12 participants used a reconstructed matrix of 128 × 128 with voxel size of 2.5 × 2.5 × 2.5 mm. The construction of structural brain networks consisted of a two-step process. First, the nodes of the network were defined using brain parcellation techniques. Secondly, the connections between nodes (i.e. edges) were estimated using probabilistic tractography (see Fig. 1). In the following we outline the details involved in each step.

First, we used the automated anatomical labeling (AAL) template to parcellate the entire brain into 90 cortical and subcortical regions (45 for each hemisphere), where each region represents a node of the brain network (Tzourio-Mazoyer et al., 2002). In addition, we created a new AALThal parcellation by combining the AAL atlas with the Oxford Thalamic Connectivity Probability Atlas (Behrens et al., 2003a, 2003b). The AALThal atlas replaces the thalamus with 7 thalamic subregions and thus has 102 cortical and subcortical regions. The parcellations were conducted in the diffusion MRI native space. The parcellation was conducted in the diffusion MRI native space. We used the Flirt tool (FMRIB, Oxford) (Jenkinson et al., 2002) to linearly coregister the b0 image in diffusion MRI space to the T1-weighted structural image. The transformed T1-weighted image was then mapped to the T1 template of ICBM152 in MNI space (Collins et al., 1994). The resulting transformation was inversed and further applied to warp the Automated Anatomical Labeling (AAL) (Tzourio-Mazoyer et al., 2002) from MNI space to the diffusion MRI native space, where interpolation used the nearest-neighbor method ensuring the preservation of discrete labeling values.

Secondly, we created the brain connectivity matrix from diffusion tensor data using our standard data pipeline (see e.g. Van Harteveld et al., 2014) which uses tools from FMRIB's Diffusion Toolbox as part of FSL (FMRIB's Software Library, http://www.fmrib.ox.ac.uk/fsl/). The various processing stages of the diffusion MRI data are specified in the following. The initial preprocessing involved coregistering the diffusion-weighted images to a reference volume using an affine

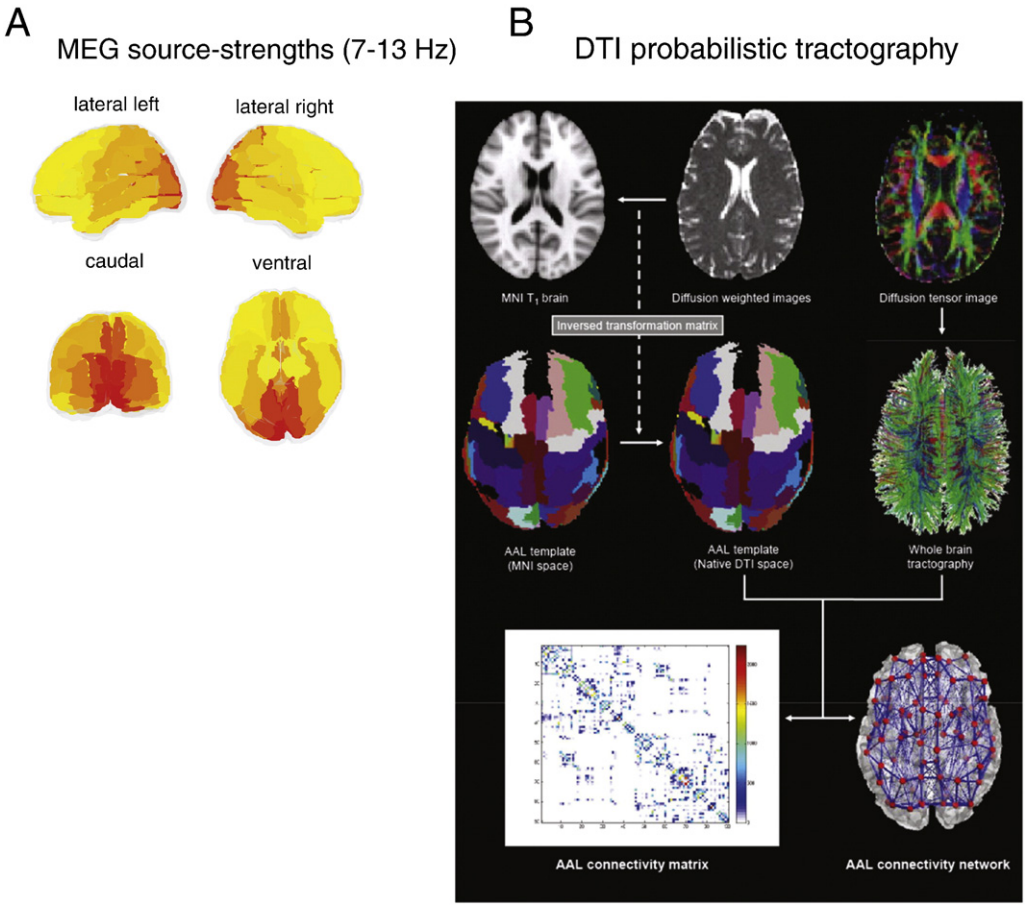

Fig. 1. Reconstruction of MEG source-strengths and DTI probabilistic tractography. A. Color-coded standard-deviations of the source-projected MEG time-series in the α frequency band (7–13 Hz) for all cortical AAL regions. The colorscale ranges from yellow to red. B. Based on T1-weighted MRI images, grey matter is segmented and parcellated using the AAL volumetric template, consisting of 90 regions-of-interest (colors are random). White-matter tracts are reconstructed from diffusion-weigthed images via estimated diffusion tensors using a probabilistic tractography algorithm. The reconstructed tracts between the (centers of) the AAL regions constitute the white-matter network used in this study.

transformation for the correction of head motion as well as eddy current induced image distortion. Following this preprocessing, we estimated the local probability distribution of fiber direction at each voxel (Behrens et al., 2003b). We then used the probtrackx algorithm allowing for automatic estimation of two fiber directions within each voxel, which can significantly improve the tracking sensitivity of non-dominant fiber populations in the human brain (Behrens et al., 2007). We estimated the connectivity probability by applying probabilistic tractography at the voxel level using a sampling of 5000 streamline fibers per voxel. The connectivity probability from a seed voxel i to another voxel j was defined by the proportion of fibers passing through voxel i that reach voxel j (Behrens et al., 2007). This was then extended from the voxel level to the region level, i.e. in a brain region consisting of n voxels, *5000n* fibers were sampled. The connectivity probability density P_{ij} from region i to region j is calculated as the number of sampled fibers in region i that connect the two regions divided by *5000n*, where n is the number of voxels in region i. The use of connectivity probability per volume unit, calculated by normalizing the connectivity probability by the number of voxels in each region, is required since the MEG data was projected onto the centers of the AAL regions, rather than onto their entire volumes. For each brain region, the connectivity probability density to each of the other 101 regions was calculated, yielding a 102×102 matrix P. Following (Cabral et al., 2011), we symmetrized the structural matrix by averaging the probability densities B_{ij} and B_{ji} for each pairs of regions (i, j), since any knowledge of directionality is absent.

To simplify the structural matrix, we excluded all thalamic segments except for the occipital segment, which projects mainly to the occipital lobe (Behrens et al., 2003a). This segment contains the lateral geniculate nucleus (LGN) which is possibly involved in the generation of posterior α (Lopes da Silva et al., 1973; Hughes et al., 2004) as well as the pulvinar, and most likely several intra-laminar nuclei (Behrens et al., 2003a). This yielded a 90×90 structural probability matrix B. We subsequently averaged B over both hemispheres yielding yielding a 45×45 connectivity matrix. The regions are listed in Table 1 (Appendix A). Justification for this comes from the fact that left and right intra-hemispheric connections are correlated with $\rho = 0.92$ ($p = 0.0000$, two-sided t-test). Furthermore, given the fact that there were no significant differences between MEG α-amplitude between homologue cortical areas (the minimum p-value over homologue cortical areas obtained from 10^4 hemispherically-randomized amplitudes equals $p = 0.7461$) we averaged the amplitudes over hemispheres. The hemispheric symmetry of α amplitudes is also evident from a correlation coefficient of $\rho = 0.97$ ($p = 0.0000$, two-sided t-test) between the amplitudes in left and right hemispheres. Fig. 1A shows the topographies of left and right cortical α-amplitudes.

Dynamical meanfield model

The electrical activity in individual AAL regions is modeled by adopting a meanfield approach to neuronal dynamics (Nunez and Srinivasan, 2006; Deco et al., 2008). Specifically, and adopting the same formalism as used in (David et al., 2006; Moran et al., 2007), each region is assumed to comprise excitatory and inhibitory neural populations. For cortical and thalamic regions, the excitatory and inhibitory populations correspond to pyramidal (PY) and inhibitory (IN) populations and thalamo-cortical (TC) and reticular (RE) populations, respectively. Membrane excitability is modeled by the function

$$S(v) = \frac{1}{1 + e^{-\rho_1 (v - \rho_2)}},$$

which converts average membrane potentials into average firing-rates. The parameters ρ_2 and ρ_1 denote the average spike-threshold and dispersion of spike-thresholds over the population, respectively. Furthermore, the populations are assumed to integrate incoming spike-rates linearly through synaptic responses parameterized by

$$h(t) = H\kappa t e^{-t\kappa},$$

where H and κ denote the synaptic efficacy and rate-constant, respectively. Efficacies and rate-constants depend on the type of synapse (excitatory or inhibitory) and on the types of pre- and post-synaptic populations (PY, IN, TC, or RE). The excitatory and inhibitory populations of a given region are coupled through a number of excitatory→inhibitory and inhibitory→excitatory synapses, which are denoted by γ_1 and γ_2, respectively.

The synaptic organization of the model is illustrated in Fig. 2A. Cortico-cortical pathways are modeled by excitatory PY → PY projections and the thalamo-cortico-thalamic loop consists of excitatory thalamo-cortical projections TC → PY and excitatory cortico-thalamic projections PY → TC which leave collaterals PY → RE to the reticular population. We thus simplify the synaptic organization and do not study the effect of TC → IN projections as done for example in (Robinson et al., 2001). The coupling strengths are assumed to be proportional to the corresponding entries of the connectivity probability density matrix B. In addition, the excitatory populations in both cortex and thalamus are driven by a constant afferent firing-rate which models non-specific background activity. We use independent global coupling strengths K_1 and K_2 for cortico-cortical and cortico-thalamo-cortical connections, respectively. Thus, K_1 corresponds to the overall strength of cortico-cortical connections and K_2 to the overall strength of feedback within the cortico-thalamo-cortical loop. They are incorporated into the model by using them as weights in the connectivity density matrix B (see Appendix B). Following previous modeling studies (Ghosh et al., 2008; Deco et al., 2009; Cabral et al., 2011; Deco and Jirsa, 2012) K_1 and K_2 are considered free parameters and are used to tune the model. Source-projected MEG signals are assumed to be proportional to the average dendritic activity of the pyramidal populations in the corresponding cortical AAL regions (Nunez and Srinivasan, 2006; Deco et al., 2008). The model equations are given in Appendix B. With some minor modifications, the parameter values are taken from (Moran et al., 2007) and are listed in Table 2 (Appendix B).

The parameter values determining the dynamics of cortical and thalamic regions were chosen to be identical and such that the excitatory populations had a stable equilibrium voltage and resonated at a frequency ≈ 10 Hz. Hence we assume that the local circuitry of all regions is tuned to resonate at α-frequency when driven by excitatory synaptic input. Fig. 2B provides an illustration. We investigated two scenarios for α-generation, namely, local generation in V1 and distributed generation throughout the cortex. An α-generator in V1 was modeled by driving the excitatory population by excitatory synaptic input, modeled as white-noise with standard deviation $\sigma = 1\ s^{-1}$. Distributed α-generation were modeled by setting $\sigma = 1\ s^{-1}$ for all cortical regions.

Results

Dynamical workingpoint

To obtain a dynamical workingpoint for the model, we first determined the models' stability boundary in the plane spanned by the cortico-cortical and thalamo-cortical connection-strengths K_1 and K_2, respectively. In terms of dynamics, restricting the workingpoint to the stable region means that we assume resting-state α-oscillations to emerge from stochastic perturbations of a stable equilibrium state, in agreement with empirical studies (Stam et al., 1999; Hindriks et al., 2011) and in line with modeling studies on fMRI resting-state dynamics (Ghosh et al., 2008; Deco et al., 2013). To determine the stability boundary, we compute the models' Jacobian at the steady-state and numerically calculate its eigenvalues (see Appendix C). Each eigenvalue λ is

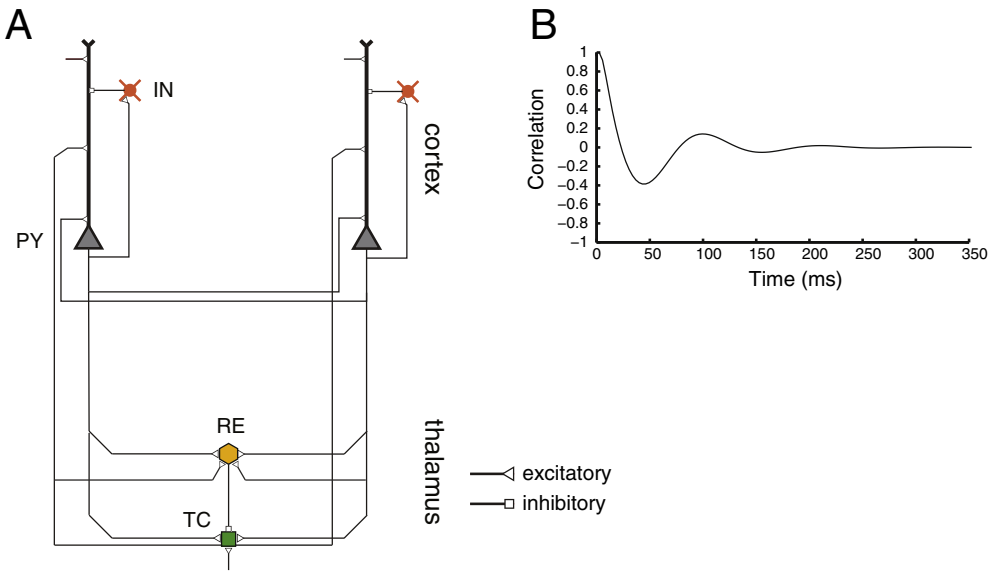

Fig. 2. Meanfield model of α-oscillations. (A) Illustration of the synaptic organization of the model. Each region-of-interest is modeled by a neural mass comprising different types of neural populations. Shown are two cortical masses, each consisting of a population of pyramidal (PY) and inhibitory interneurons (IN) and a thalamic mass, consisting of a population of thalamo-cortical relay (RE) and thalamic reticular (RE) neurons. Synaptic connections are illustrated by black lines connecting the different populations. Connections that end with a triangle and square denote excitatory and inhibitory connections, respectively. Cortical regions are coupled via excitatory PY → PY projections and cortex and thalamus are coupled via excitatory TC → PY and PY → TC projections which leave collaterals to reticular neurons (RE). Both PY and TC populations are driven by a constant afferent firing-rate. (B) Autocorrelation function of the cortical pyramidal (PY) population in a cortical region-of-interest when it is isolated from all other regions-of-interest. The autocorrelation function is the inverse Fourier transform of the power spectrum, hence determines the resonance-strength of the population for synaptic inputs of all frequencies. Note that it behaves as a damped oscillation with period $\approx$100 ms, corresponding to α-frequency of $\approx$10 Hz. The oscillations emerge from the inhibitory feedback loop between the PY and IN populations.

complex-valued and describes the resonance behavior of one of the state-variables. Specifically, the response of the state-variable upon an instantaneous perturbation is an exponentially damped oscillation e^{λ}, where the damping-rate $Re(\lambda)$ and frequency $Im(\lambda)$ describe the characteristic time-scale and angular frequency of the response. The stable regime corresponds to the values of (K_1, K_2) for which the damping-rate $Re(\lambda) < 0$ for all state-variables. Fig. 3A shows color-coded damping-rate and frequency of the least-damped eigenvalue as a function of (K_1, K_2). The boundary in the images corresponds to the stability boundary. Note that approaching the stability boundary leads to increased \alpha-frequency. When crossed, the system destabilizes through a supercritical Hopf bifurcation, giving rise to self-sustained α-oscillations, a scenario that is more likely to be related to epileptic dynamics, in particular tonic-clonic seizures (Robinson et al., 2002; Breakspear et al., 2006).

To find a dynamical workingpoint (K_1^*, K_2^*), we placed a generator in V1 and computed the Pearson correlation coefficient between the predicted and observed cortical α-amplitudes, that is, between the standard-deviations of the modeled time-series and the corresponding source-projected MEG time-series filtered in the α frequency band. We did this as a function of (K_1, K_2) in the entire stable regime. The predicted amplitudes were computed semi-analytically (see Appendix D). The correlation coefficients reached a local maximum of $\rho = 0.80$ at $(K_1^*, K_2^*) = (66, 40)$, which we chose as the dynamical working point. The dynamical workingpoint is designated in Fig. 3B (left-hand figure) by a white dot. Importantly, the fact that the model performs best well away from the horizontal and vertical boundaries, which correspond to the absence of cortico-cortical and thalamo-cortical connections respectively, suggests the involvement of both cortico-cortical as well as thalamo-cortical pathways in shaping the distribution of cortical α-amplitudes. Also note that the model performs best for a value of (K_1, K_2) that lies in the interior of the stability region, as opposed to a best fit on the instability boundary. This shows that the chosen workingpoint corresponds to a well-defined best fit.

Since in the above simulations, V1 displayed much larger oscillations than other regions—in contrast to the observed oscillations—we excluded V1 before computing the correlation coefficients. This discrepancy between model and data might be caused be passive propagation of the magnetic field generated by cortical sources leading to an offset in the amplitudes of the source-projected MEG signals which is absent in the simulated data. Alternatively, it could be that a single generator in V1 is too restricted and that the data may be better explained by assuming multiple α-generators. To test this possibility, we placed a generator in every cortical region and repeated the above assessment of how well the observed α-amplitudes are predicted by the model. The result is shown in Fig. 3B (right-hand figure). The figure shows that although there is a well-defined maximum in model performance, the maximal correlation coefficient is low ($\rho = 0.21$).

Fig. 3B shows that in both model simulations, the best fit is obtained for non-zero cortico- and thalamo-cortical coupling strengths, which suggest involvement of both types of pathways in coordinating cortical α-oscillations. However, when the workingpoints (white dots) are projected to the cortico-cortical axis, the correlation with the data remains high, while projection to the thalamo-cortical axis yields substantially lower correlations. Thus, in both simulations, cortico-cortical pathways contribute more to structuring α-amplitudes than thalamo-cortical connections do. This is in agreement with the findings reported in (Lopes Da Silva et al., 1980) using local field potentials simultaneously recorded from visual cortex and thalamus. Using partial coherence analysis, it was found that cortico-cortical connections contributed more to the coherence between α-oscillations in different cortical regions than thalamo-cortical connections did.

Spatial extent of posterior alpha oscillations

Fig. 4A shows the scatterplot of the observed α-amplitudes versus those predicted by the model in the chosen workingpoint (K_1^*, K_2^*). They are correlated with Pearson correlation coefficient $\rho = 0.80$. To determine the spatial extent of posterior α-oscillations, we selected the regions that were anatomically connected to V1 with a connection strength $\geq h$ and computed the Pearson correlation coefficient between the predicted and observed amplitudes within the selected regions. The regions were determined by computing the correlation coefficients as a function of h and subsequently selecting the value of h for which the

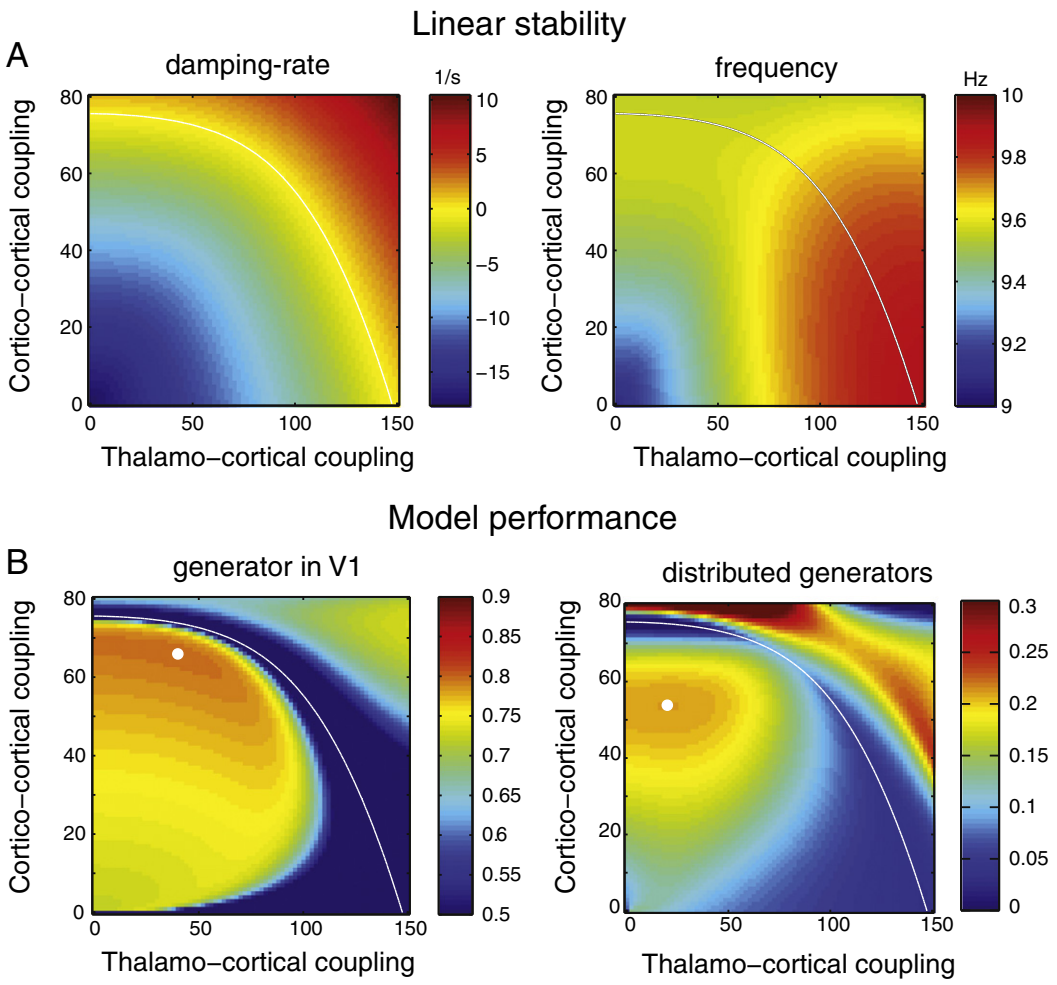

Fig. 3. Linear stability and dynamical workingpoint. A. Left: Damping-rate of the least-damped eigenvalue as a function of cortico-cortical and thalamo-cortical coupling strength K_1 and K_2. Right: Frequency of the least-damped eigenvalue as a function of cortico-cortical and thalamo-cortical coupling strength K_1 and K_2. B. Left: Pearson correlation coefficients between the observed α-amplitudes and those predicted by the model by assuming a single α-generator in the Calcarine sulcus (V1). The correlation is maximal at $(K_1^*, K_2^*) = (66, 40)$ and is denoted by a white dot. Right: Pearson correlation coefficients between the observed α-amplitudes and those predicted by the model by assuming α generators to be distributed throughout the cortex. The correlation is maximal at $(K_1^*, K_2^*) = (66, 40)$ and is denoted by a white dot. The correlation coefficients in the right-hand-side figure were predicted by the model in which α-generators were assumed to be distributed throughout the cortex. The correlation is maximal around $(K_1^*, K_2^*) = (53, 20)$ and is denoted by a white dot. Note the difference in colorscaling between the figures. In all figures, K_1 and K_2 range from 0 to 80 and from 0 to 150, respectively, in steps of 1 and 2, respectively and the curved white boundary coincides with the (linear) stability boundary.

correlation coefficient attained a local maximum. This gave a threshold of $h = 0.03$. Propagation was found to pervade the entire occipital lobe, with extensions to posterior–parietal and temporal regions. Specifically, α propagated to the inferior, medial, and superior occipital gyri (IOG, MOI, SOG), cuneus (CUN), lingual gyrus (LING), posterior cingulate gyrus (PCG), hippocampal gyrus (HPG), parahippocampal gyrus (PHG), fusiform gyrus (FFG), and precuneus (PCUN) and are displayed on a glass brain in Fig. 4B.

In the sequel, we collectively refer to these regions as the *posterior α-network*. Note that the posterior \alpha-network roughly comprises visual cortical regions, including the dorsal and ventral projection systems, and thus reinforces the notion of posterior α-oscillations as intrinsic oscillations of the visual system. The Pearson correlation coefficient between predicted and observed amplitudes within the posterior α-network was $\rho = 0.93$, which demonstrates the model's ability to reproduce the relative α-amplitudes. The amplitudes within the visual system are denoted by red dots in Fig. 4A. Interestingly, the regions comprising the posterior \alpha-network largely coincide with those in which resting-state BOLD-fluctuations are (negatively) correlated with simultaneously recorded posterior α-power fluctuations (Feige et al., 2005). This might suggest that resting-state BOLD-fluctuations within the visual system are driven by fluctuations in V1.

Involvement of primary visual pathways

If the hypothesis that posterior α-oscillations propagate from V1 to higher-order visual areas through excitatory white-matter pathways is correct, one might suspect a positive correlation between α-amplitudes of regions within the posterior α-network and corresponding structural connection-strengths to V1. Fig. 5A, left-hand-side, shows the scatterplot between predicted posterior α-amplitudes and corresponding connection-strengths, indeed predicting a positive correlation. The correlation coefficient between observed α-amplitudes and connection-strengths to V1 was $\rho_{\alpha,sc} = 0.95$ ($p < 0.0001$, two-sided t-test), thereby confirming this prediction.

To factor out spurious correlations due to (weak) dependence of observed α-amplitudes and connection-strengths to V1 on Euclidean distance to V1 ($\rho_{\alpha,dist} = -0.80$, $p = 0.0050$ and $\rho_{sc,dist} = -0.71$, $p = 0.0204$, two-sided t-tests), which also holds for the predicted amplitudes, we conditioned $\rho_{\alpha,sc}$ on Euclidean distance, which yielded a partial correlation coefficient of $\rho_{\alpha,sc|dist} = 0.89$ ($p = 0.0012$, two-sided t-test), which shows that the correlation between α-amplitude and connection-strength cannot be explained by their common dependence of distance to V1. In contrast, $\rho_{\alpha,dist}$ vanished when conditioned on connection-strength ($\rho_{\alpha,dist|sc} = -0.57$, $p = 0.1112$, two-sided

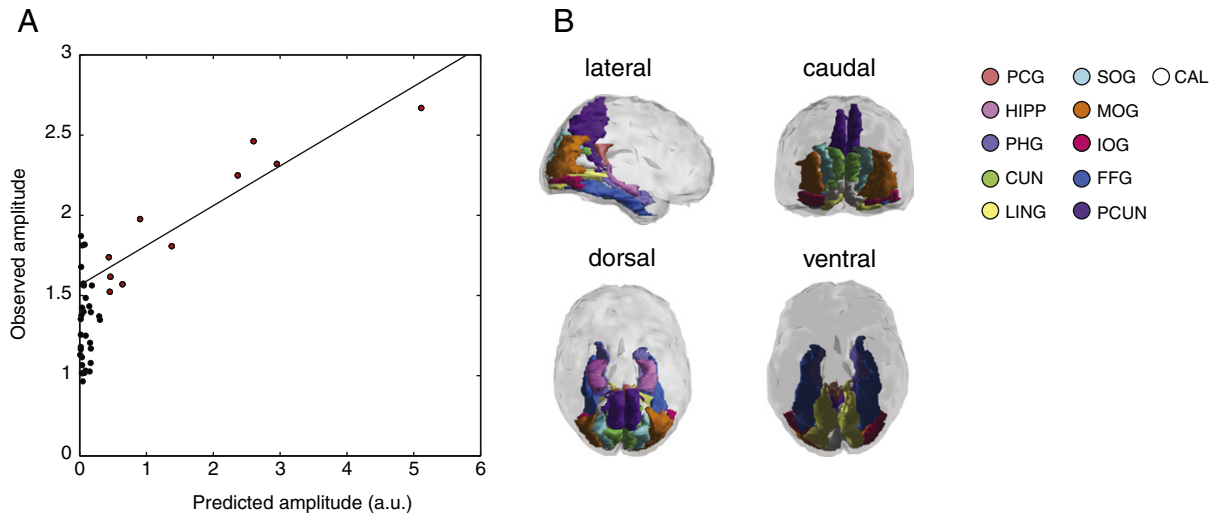

Fig. 4. Model performance and spatial extent of posterior α-oscillations. A. Scatterplot of observed versus predicted α-amplitudes for the model in the workingpoint (K_1^*, K_2^*). Each dot corresponds to a cortical region. The dots that correspond to regions whose amplitude could be explained by the model are colored in red. Together, these regions are referred to as the posterior α-network. The variance of the predicted amplitudes is scaled to unity. B. Glass-brain views of the posterior α-network. It comprises the inferior, medial, and superior occipital gyri (IOG, MOI, SOG), cuneus (CUN), lingual gyrus (LING), posterior cingulate gyrus (PCG), hippocampal gyrus (HPG), parahippocampal gyrus (PHG), fusiform gyrus (FFG), and precuneus (PCUN). Colors are insignificant and merely serve to delineate the different regions.

t-test), which shows that the correlation between α-amplitude and distance reflects the dependence of structural connection-strength to V1 on distance.

If α-oscillations propagate from V1 to higher-order visual areas, we would expect a positive correlation between α-amplitudes in higher-order visual regions and their functional connection strength to V1.

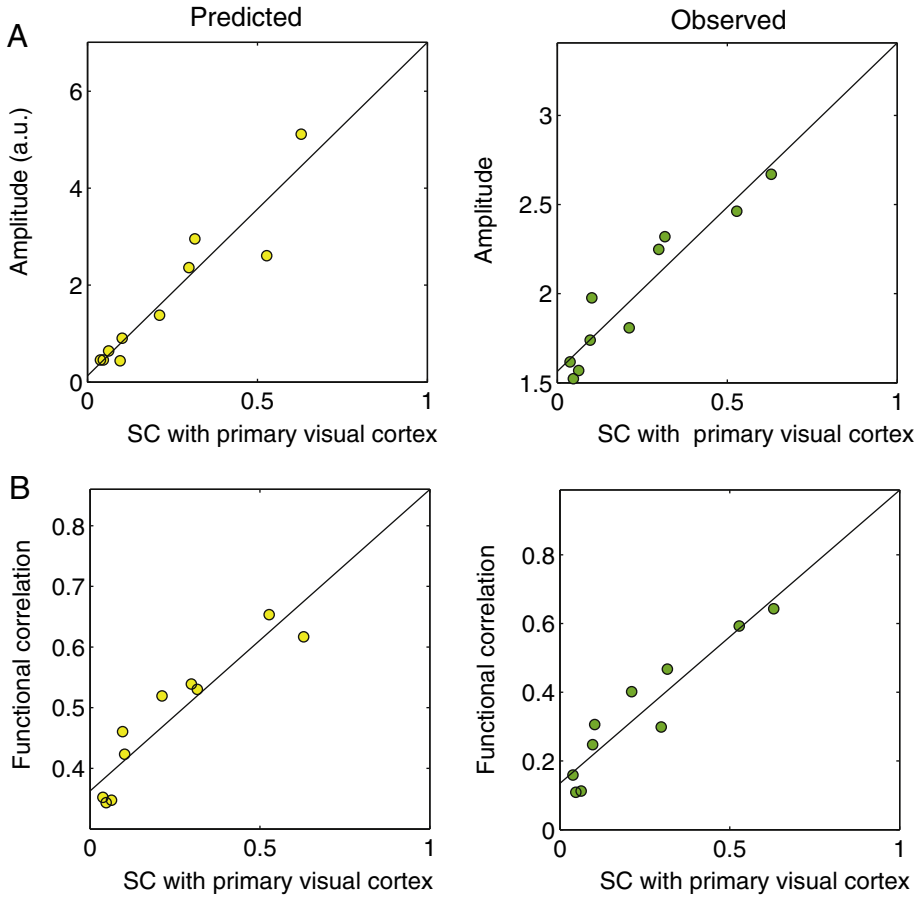

Fig. 5. Correlations between α-amplitude and structural and functional connections. A. Scatterplot of the predicted (left) and observed (right) α-amplitudes of regions within the visual α-network versus corresponding structural connection-strengths with V1. B. Scatterplots of predicted (left) and observed (right) α-amplitudes of regions within the visual α-network versus corresponding functional connection-strengths with V1. Observed functional correlations were quantified by bandlimited power (BLP) correlations, that is, by pair wise Pearson correlation coefficients between the Hilbert envelopes of the source-projected MEG signals. Superimposed are regression lines obtained from a linear least-square fit. Predicted amplitudes have been normalized to unit standard-deviation.

This is illustrated in Fig. 5B, left-hand-side, which shows that the model indeed predicts the existence of such a correlation. Functional correlations from the model were measured by the Pearson correlation coefficients between the theoretical time-series and were computed semi-analytically from the linearized model equations (see Appendix E). Fig. 5B, right-hand-side, shows that this prediction holds for the data as well ($\rho_{fc,sc} = 0.94, p = 0.0001$, two-sided t-test). Observed functional correlations were quantified by the bandlimited power (BLP) correlations between the source-projected MEG signals, that is, by the Pearson correlation coefficients between the corresponding Hilbert envelopes. Although the predicted functional correlations were quantified differently than in the model, allowing for a semi-analytical computation without the need for numerical simulations, the two kinds of correlations are approximately proportional within the model, justifying their use in linear correlation analysis. To factor out spurious correlations due to the negative dependence of functional correlation on distance ($\rho_{fc,dist} = -0.87$, $p = 0.001$, two-sided t-test) we conditioned the correlation on Euclidean distance. The partial correlation remained significant ($\rho_{fc,sc|dist} = 0.92$, $p = 0.0004$, two-sided t-test) showing that $\rho_{fc,sc}$ can only partially be explained by a common dependence of functional correlation and connection-strength of distance.

Discussion

In this study we combined MEG source-modeling (Woolrich et al., 2011), DTI probabilistic tractography, connectivity-based thalamic segmentation (Behrens et al., 2003a, 2003b, 2007), and biophysical modeling to investigate the role of white-matter pathways in coordinating α-oscillations in human cortex at rest. We focused on two scenarios for the generation of α-oscillations, namely, local generation within the Calcarine sulcus (V1) as suggested by MEG inverse-modeling studies (Salmelin and Hari, 1994; Hari and Salmelin, 1997; Ciulla et al., 1999) and distributed generation of α-oscillations throughout the cortex. Both scenarios suggested that α-oscillations propagate through cortico-cortical as well as thalamo-cortical pathways, although cortico-cortical pathways seemed to play a larger role, in line with local field potential recordings in dogs (Lopes Da Silva et al., 1980). The assumption of a single α-generator in V1 however, led to a much better fit with the data than the distributed scenario. While this finding does not rule out the existence of distributed α-generators, nor the existence of a single spatial eigenmode (Nunez and Srinivasan, 2006), it at least suggests that V1 plays a central role in coordinating posterior α-oscillations. Furthermore, the models' ability of predicting MEG source-strengths of α-oscillations was limited to the occipital lobe and parts of the temporal and medial-posterior parietal lobe, namely the inferior, medial, and superior occipital gyri, cuneus, lingual gyrus, posterior cingulate gyrus, hippocampal gyrus, parahippocampal gyrus, fusiform gyrus, and precuneus. This reinforces the notion that posterior α-oscillations are intrinsic to the visual system. Both the anatomical and functional connections to V1 correlated with the source-strengths of α-oscillations within this network, as predicted by the model.

Equivalent-dipole modeling of resting-state MEG α-oscillations has shown that the strongest α-sources are located in the calcarine sulcus (V1) and occipito-parietal fissure. The relative source-strengths however, differ from subject to subject (Salmelin and Hari, 1994; Hari and Salmelin, 1997; Ciulla et al., 1999). In line with these observations, the group-averaged MEG source-strength of our data was highest in the calcarine sulcus, followed by the cuneus, which extends into the medial part of the posterior wall of the occipito-parietal fissure. However, both in the data and model, cortical source-strengths only correlated with white-matter connections to the calcarine sulcus and not with the cuneus. Since calcarine was most strongly connected to the cuneus, this suggests that propagation of oscillations within the calcarine sulcus might contribute to the strong α-sources within the occipito-parietal fissure.

Since for all subjects, the α-amplitudes in the calcarine sulcus and occipito-parietal fissure were of similar magnitude, we suspect that the estimated MEG source-strengths are attenuated by partial cancelation of coherent oscillations in opposite banks of the calcarine sulcus 2 (Salmelin and Hari, 1994; Hari and Salmelin, 1997; Nunez and Srinivasan, 2006). This remains speculative however, and the use of MEG alone might not be sufficient to provide a definite answer, because MEG is primarily sensitive to the tangential component of current sources (Hamalainen et al., 1993). A more complete picture of the organization of cortical α-sources likely has to come from combined EEG-MEG source-imaging methods (Baillet et al., 1999) as they exploit the complementary information of MEG and EEG, which is primarily sensitive to the radial component of current sources. In addition to combining EEG and MEG, the inverse-solution space might be reduced further by assuming the current densities to be restricted to the cortical surface and their orientation to be perpendicular to it (Dale and Sereno, 1993). This would, however, require using a more fine-grained parcellation of the cortical surface and higher-resolution structural matrices.

Several studies have shown that posterior α-oscillations can be actively increased and decreased in visual attention paradigms in a retinotopically specific way (Yamagishi et al., 2005; Kelly et al., 2006; Rihs et al., 2007; Jensen et al., 2010; Capilla et al., 2012) both in primary as well as in higher-order visual areas (Jokisch and Jensen, 2007; Snyder and Foxe, 2010). Based on our results, we might speculate that in resting-state, propagation of α from lower to higher-order visual areas might provide a default organization of visual cortex in which modulation of α in V1 induces coherent modulations of α in higher-order visual areas through retinotopically-organized pathways. Through such a mechanism, retinotopical-specific priming of V1 might automatically prime corresponding locations in higher-order areas. Such a mechanism could coexist together with top-down modulating signals, which are known or be broadcasted by several regions, most notably frontal and parietal areas (Kelly et al., 2006) as well as several subcortical nuclei (Feige et al., 2005), in particular the pulvinar (Shipp, 2003; Saalmann et al., 2012), whose connections to visual cortex are known to be organized in a retinotopic way (Shipp, 2003). Most likely, the spatio-temporal organization of posterior α emerges from coordinated modulating influences through both top-down and bottom-up cortico-cortical and pulvinar-cortical pathways.

In this study, we focused on occipital \alpha-oscillations (Ciulla et al., 1999), which are but one example of a family of $\approx$10 Hz oscillations that can be recorded from human neocortex. Besides occipital \alpha-oscillations, which are associated with the visual system, *mu* and *tau* oscillations are associated with the somato-sensory and auditory systems, respectively (Baar et al., 1997; Hari and Salmelin, 1997). In addition, a line of experiments suggests the existence of several types of oscillations within the classical \alpha-frequency band (7–13 Hz) that might subserve different cognitive roles (Klimesch et al., 1998; Klimesch, 1999; Lopes Da Silva, 2013). An interesting direction for future research therefore, would be to study the distribution of generators of these different kinds of \alpha-oscillations, how they propagate through white-matter pathways, and interact with one another and with occipital \alpha-oscillations through shared anatomical pathways.

The data used in this study are limited in several respects. The most important limitation is that thalamic voxels were classified based on the abundance of their structural connections with the major anatomical regions in cerebral cortex, namely occipital, parietal, temporal, frontal, motor, pre-motor, and somato-sensory regions, hence did not allow delineation of the lateral geniculate nucleus (LGN) and the isolation of higher-order visual thalamic nuclei (Behrens et al., 2003a). As a consequence, our findings do not allow to distinguish the different scenarios of α-generation, namely

generation in cortical (Liley et al., 1999) or thalamic (Lopes da Silva et al., 1974; Hughes et al., 2004) tissue, or reverberation within thalamo-cortical loop (Robinson et al., 2001; Rennie et al., 2002), nor allows to assess the role of higher-order thalamic nuclei in modulation of cortical α-oscillations (Feige et al., 2005; Saalmann et al., 2012). A more fine-grained structural segmentation of thalamus might allow for a more detailed study of the role of different thalamic nuclei in generation and modulation of cortical α. A second limitation is that the MEG recordings and MRI scans were obtained from different subject groups. Remarkably, the observed correlations between the anatomical and functional organization of posterior α-oscillations on the group-level reflect their robustness. Paired MEG-DTI recordings obtained in a subsequent study will allow further validation of the findings reported in the current study.

Although the model was able to reproduce the relative amplitudes of \alpha-sources in visual cortex, there remains a discrepancy between the predicted and observed amplitudes. Specifically, the observed amplitudes have an off-set which is absent in the predicted amplitudes (see Fig. 4A). Moreover, and possibly related, the predicted amplitude in V1 is relatively large as compared to the amplitudes in higher-order visual regions. A possible explanation for this is the existence of multiple α-generators, which would lead to a smoother spatial arrangement of the amplitudes (Robinson et al., 2001, 2002). Assuming multiple α-generators in the current model, however, did not lead to a good fit with the data (see Fig. 3D). Possibly, the true scenario is somewhere in between these two extremes and \alpha-generation has both focal and distributed characteristics. An alternative explanation however, is that the off-set is caused by passive propagation of the generated magnetic field, which has not been incorporated in the model.

The issue raised in the previous paragraph will be better investigated by treating the cortex as a spatially continuous structure (a sheet) instead of a discrete network of regions as done in this study. In modeling terms, this means that the neural mass model needs to be extended to a neural field model that takes into account not only the topology of cortico-cortical axons, which is partially homogeneous and partially highy specific, but also the spatial arrangement of local intra-cortical axons (Robinson et al., 1997; Deco et al., 2008). Such an approach however, requires MEG source-modeling to be restricted to a high-resolution triangulation of the cortical surface (Jirsa et al., 2002), which is challenging in itself. Moreover, the computational load of simulating neural field models on such high-resolution representations on human cortex is relatively high (Bojak et al., 2011). Steps in this direction however, have already been taken (Bojak et al., 2010) and are facilitated by open source simulation packages such as The Virtual Brain (www.thevirtualbrain.org).

As mentioned above, this study exclusively focused on the role of white-matter pathways and ignored the role of local intra-cortical axons in shaping the spatio-temporal behavior of cortical \alpha-oscillations. In a recent paper (Hindriks et al., 2014), Hindriks et al. described a complementary approach and exclusively focused on the role of intra-cortical connectivity in shaping posterior \alpha-oscillations. In that study, the authors used EEG data-analysis and forward modeling to argue that posterior \alpha-oscillations propagate through the cortex via intra-cortical axons. Moreover, they estimated that the spatial extent of such propagating \alpha-sources is limited to several centimeters. These two studies, each of which stresses a complementary aspect of the spatio-temporal dynamics of cortical \alpha, suggest a view of \alpha as comprising a multitude of local and intra-cortically propagating sources that are coordinated or synchronized through white-matter fiber pathways. This is reminiscent of the spatio-temporal behavior of gamma oscillations in sensory cortices, which locally behave as traveling waves (Freeman et al., 2000), but also can become synchronized over large distances. We expect that the use of neural field models with heterogeneous white-matter topologies (Jirsa and Kelso, 2000; Bojak et al., 2011) will provide a suitable framework to study how local intra-cortical propagation and long-range synchronization interact to shape the spatio-temporal dynamics of cortical oscillations.

Acknowledgments

The authors thank Ole Jensen from the Donders Institute for Brain, Cognition, and Behaviour, Nijmegen, The Netherlands and Wessel van Wieringen from the VU University Amsterdam, The Netherlands for their valuable conversations regarding this manuscript. In addition, the authors like to thank the reviewers for their constructive comments.

GD was supported by the ERC Advanced Grant: DYSTRUCTURE (n. 295129), by the Spanish Research Project SAF2010-16085 and by the CONSOLIDER-INGENIO 2010 Program CSD2007-00012, and the FP7-ICT BrainScales (n. 269921). MLK was supported by the ERC Consolidator Grant: CAREGIVING (n. 615539) and the TrygFonden Charitable Foundation. The authors declare no competing financial interests.

Appendix A. Regions of interest

Table 1
Descriptions and abbreviations of the AAL regions used in this study.

Region	Abbr
Precentral	PreCG
Frontal Sup	SFGdor
Front Sup Orb	ORBsup
Front Mid	MFG
Front Mid Orb	ORBmid
Front Inf Ope	IFGoperc
Front Inf Tri	IFGtriang
Front Inf Orb	ORBinf
Rolandic Oper	ROL
Supp Motor Ar	SMA
Olfactory	OLF
Front Sup Med	SFGmed
Front Med Orb	ORBmid
Rectus	REC
Insula	INS
Cingulum Ant	ACG
Cingulum Mid	DCG
Cingulum Post	PCG
Hippocampus	HPG
ParaHippocamp	PHG
Amygdala	AMYG
Calcarine	CAL
Cuneus	CUN
Lingual	LING
Occipital Sup	SOG
Occipital Mid	MOG
Occipital Inf	IOG
Fusiform	FFG
Postcentral	PoCG
Parietal Sup	SPG
Parietal Inf	IPL
SupraMarginal	SMG
Angular	ANG
Precuneus	PCUN
Paracentr Lob	PCL
Caudate	CAU
Putamen	PUT
Pallidum	PAL
Thalamus	THA
Heschl	HES
Temporal Sup	STG
Tempr Pol Sup	TPOsup
Temporal Mid	MTG
Tempr Pol Mid	TPOmid
Temporal Inf	ITG

Appendix B. Model equations

The state-variables of the k-th region ($k = 1, \cdots, N$) are the average membrane potentials of excitatory and inhibitory neurons, denoted by V_e^k and V_i^k, respectively. They satisfy the following equations:

$$V_e^k(t) = -h_\mathrm{I} \otimes \left[\gamma_{ie}^k Q_i^k(t) + \sum_{l\neq k} \beta_{ie}^{lk} Q_i^l(t)\right] + h_\mathrm{E} \otimes \left[\sum_{l\neq k} \beta_{ee}^{lk} Q_e^l(t) + p^k(t)\right],$$

$$V_i^k(t) = -h_\mathrm{I} \otimes \left[\gamma_{ii}^k Q_i^k(t) + \sum_{l\neq k} \beta_{ii}^{lk} Q_i^l(t)\right] + h_\mathrm{E} \otimes \left[\sum_{l\neq k} \beta_{ei}^{lk} Q_e^l(t) + \gamma_{ei}^k Q_e^k(t)\right],$$

where $\otimes$ denotes temporal convolution, h_E and h_I denote the average excitatory and inhibitory post-synaptic potentials, respectively, γ_{pq}^k denotes the number of synaptic contacts from neurons of type p to neurons of type q within region k, and β_{pq}^{lk} denotes the number of synaptic contacts from neurons of type p within region l to neurons of type q within region k, for $k \neq l$. Note that the terms γ_{pq}^k and β_{pq}^{lk} specify the coupling structure *within* and *between* regions, respectively. Furthermore, $Q_p^l(t) = S(V_p^l(t))$ denotes the average firing-rate of neurons of type p in region l at time t. Moreover, $p^k = \overline{p}^k + \sigma^k \xi^k(t)$ models the afferent input to region k, which is comprised of a constant firing-rate $\overline{p}^k$ and a fluctuating term $\sigma^k \xi^k(t)$ that models the complicated afferent input under resting-state conditions by a white-noise process. We assume that the incoming fluctuations to different regions are uncorrelated, that is, $<\xi^k \xi^l> = \delta_{kl}$. The parameter values are listed in Table 2.

To go from these general equations to the specific thalamo-cortical model described in Dynamical meanfield model, we distinguish two types of excitatory neuron types, namely cortical pyramidal (PY) neurons, denoted by subscript p, and thalamo-cortical relay (RE) neurons, denoted by subscript t. We also distinguish two types of inhibitory neurons, namely cortical inhibitory (IN) neurons, denoted by subscript i, and thalamic reticular (RE) neurons, denoted by subscript r. The synaptic organization of these neuron types is illustrated in Fig. 2 (Dynamical meanfield model). The coupling between cortical pyramidal neurons of cortical regions l and k is assumed to by symmetric, that is, $\beta_{\mathrm{pp}}^{lk} = \beta_{\mathrm{pp}}^{kl}$, where $k \neq l$ index the cortical regions. Moreover, their values are taken equal to the DTI-derived connection probability density b_{kl}. Thus, $\beta_{\mathrm{pp}}^{kl} = K_1 b_{kl}$, where b_{kl} is the (k, l)-th entry of the connection probability density matrix B (see Diffusion tensor imaging) and K_1 is a dimensionless global cortico-cortical scaling factor. The coupling between cortex and thalamus is specified by the terms β_{pr}^{kl}, β_{pt}^{kl}, and β_{tp}^{lk}, which are all taken equal for given cortical indices k and thalamic indices l and are fixed by the corresponding DTI-derived thalamo-cortical connection probability densities and a dimensionless global thalamo-cortical scaling factor K_2.

Table 2
Descriptions, symbols, and nominal values of the model parameters.

Parameter	Symbol	Nominal value
Average spike-threshold	ρ_2	1 mV
Dispersion of spike-thresholds	ρ_1	2 mV^{-1}
Efficacy of PY → IN synapses	H_{pp}	4 mV
Efficacy of IN → PY synapses	H_{ip}	32 mV
Efficacy of PY → TC synapses	H_{pt}	8 mV
Efficacy of PY → RE synapses	H_{pr}	0.4 mV
Efficacy of TC → PY synapses	H_{tp}	4 mV
Efficacy of RE → TC synapses	H_{rt}	32 mV
Efficacy of TC → RE synapses	H_{tr}	4 mV
Excitatory synaptic rate-constant	κ_e	162.5 s^{-1}
Inhibitory synaptic rate-constant	κ_i	$\kappa_e/4$ s^{-1}
Number of synaptic contacts excitatory→inhibitory	γ_1	64
Number of synaptic contacts inhibitory→excitatory	γ_2	64
Afferent firing-rate into region k	$\overline{p}^k$	270 s^{-1}
Standard-deviation of p in region k	σ^k	0 or 1 s^{-1}
Global cortico-cortical coupling	K_1	≥ 0
Global thalamic feedback	K_2	≥ 0

Appendix C. Linear stability

Linear stability was assessed by rewriting the model equations as a system of N 8-dimensional coupled first-order stochastic differential equations, which were obtained by rewriting the convolutions $h_\mathrm{E} \otimes$ and $h_\mathrm{I} \otimes$ as second-order differential operators. In this form, the dynamics of region k are governed by

$$\begin{aligned}
\dot{V}_{e,1}^k(t) &= U_{e,1}^k(t),\\
\dot{U}_{e,1}^k(t) &= -2\kappa_\mathrm{E} U_{e,1}^k - \kappa_\mathrm{E}^2 V_{e,1}^k + \kappa_\mathrm{E} H_\mathrm{E}\left[p^k(t) + \sum_{l\neq k} \beta_{ee}^{l,k} Q_e^l(t))\right],\\
\dot{V}_{e,2}^k(t) &= U_{e,2}^k(t),\\
\dot{U}_{e,2}^k(t) &= -2\kappa_\mathrm{I} U_{e,2}^k - \kappa_\mathrm{I}^2 V_{e,1}^k + \kappa_\mathrm{I} H_\mathrm{I}\left[\gamma_{ie}^k Q_i^k(t) + \sum_{l\neq k} \beta_{ee}^{l,k} Q_i^l(t))\right],\\
\dot{V}_{i,1}^k(t) &= U_{i,1}^k(t),\\
\dot{U}_{i,1}^k(t) &= -2\kappa_\mathrm{E} U_{i,1}^k - \kappa_\mathrm{E}^2 V_{i,1}^k + \kappa_\mathrm{E} H_\mathrm{E}\left[\gamma_{ei}^k Q_e^k(t) + \sum_{l\neq k} \beta_{ei}^{l,k} Q_e^l(t))\right],\\
\dot{V}_{i,2}^k(t) &= U_{i,2}^k(t),\\
\dot{U}_{i,2}^k(t) &= -2\kappa_\mathrm{I} U_{i,2}^k - \kappa_\mathrm{I}^2 V_{i,1}^k + \kappa_\mathrm{I} H_\mathrm{I}\left[\gamma_{ii}^k Q_i^k(t) + \sum_{l\neq k} \beta_{ii}^{l,k} Q_i^l(t))\right],
\end{aligned}$$

where $V_e = V_{e,1} - V_{e,2}$ and $V_i = V_{i,1} - V_{i,2}$, H_E and H_I denote the efficacy of excitatory and inhibitory synapses, respectively, and $\cdot$ denotes taking the derivative with respect to time t. The associated system of steady-state equations, obtained by setting all derivatives to zero, was solved numerically, and the solutions are used to evaluate the systems' Jacobian at the steady-state.

Appendix D. Source-strengths

Assuming the noise-driven fluctuations about the steady-state to be small, the model equations can be linearized about the steady-state and the fluctuations are found to obey the following equations in the Laplace domain:

$$V_e^k = -L_\mathrm{I}\left[\gamma_{ie}^k G_i^k V_i^k + \sum_{l\neq k} \beta_{ie}^{lk} G_i^l V_i^l\right] + L_\mathrm{E}\left[\sum_{l\neq k} \beta_{ee}^{lk} G_e^l V_e^l + \sigma^k\right],$$

$$V_i^k = -L_\mathrm{I}\left[\gamma_{ii}^k G_i^k V_i^k + \sum_{l\neq k} \beta_{ii}^{lk} G_i^l V_i^l\right] + L_\mathrm{E}\left[\sum_{l\neq k} \beta_{ei}^{lk} G_e^l V_e^l + \gamma_{ei}^k G_e^k V_e^k\right],$$

where

$$G_e^k = \frac{dS}{dv}\left(\overline{V}_e^k\right)$$

denotes the average gain of excitatory neurons in region k and similarly for inhibitory neurons, and where

$$L_\mathrm{E}(s) = \frac{H_\mathrm{E} k_\mathrm{E}}{(s + k_\mathrm{E})^2},$$

denotes the average transfer function of excitatory synapses and similarly for inhibitory synapses.

To solve this system of equations for the state vector $V = (V_e^1, V_i^1, \cdots, V_e^N, V_i^N)'$, we write M_1 for the blockdiagonal matrix with k-th block given by

$$\begin{pmatrix} 0 & -\gamma_{ie}^k G_i^k L_\mathrm{I} \\ -\gamma_{ei}^k G_e^k L_\mathrm{E} & -\gamma_{ii}^k G_i^k L_\mathrm{I} \end{pmatrix}$$

and M_2 for the blockmatrix with (k, l)-th block given by

$$\begin{pmatrix} \beta_{ee}^{lk} G_e^l L_E & -\beta_{ie}^{lk} G_i^l L_I \\ \beta_{ei}^{lk} G_e^l L_E & -\beta_{ii}^{lk} G_i^l L_I \end{pmatrix},$$

for $l \neq k$. Note that M_1 and M_2 relate to the local and global coupling structure, respectively. Furthermore, by defining $\Sigma = (\sigma^1 L_E, \cdots, \sigma^N L_E)'$ and $M = M_1 + M_2$, the Laplace domain equations can be written in matrixform as

$$V(s) = MV(s) + \Sigma(s),$$

from which we obtain

$$V(s) = (I - M(s))^{-1}\Sigma(s),$$

where I denotes the identity matrix of size $2N$. The entries of $V(s)$ correspond to the transfer functions of the excitatory and inhibitory populations in the different regions. If the steady-state is stable, the Fourier spectra of the excitatory populations can be calculated by setting $s = i\omega$. Thus, the Fourier spectra of the MEG signals from the k-th region are modeled by

$$V_{MEG}^{(k)}(\omega) = V_e^k(i\omega).$$

Using the assumption that the afferent fluctuations of the different regions are uncorrelated, the MEG cross-spectral matrix is given by

$$S_{MEG}(\omega) = V_{MEG}(\omega) D_P(\omega) (V_{MEG}(\omega) D_P(\omega))^{\dagger},$$

where $D_P(\omega)$ denotes the diagonal matrix with the vector $P(\omega)$ as the diagonal and † denotes conjugate-transpose. This expression simplifies to

$$S_{MEG}(\omega) = \sigma^2 V_{MEG}(\omega) V_{MEG}(\omega)^{\dagger},$$

because $D_P(\omega)$ is a diagonal matrix. The strength A_k of region k, as measured by its standard-deviation, is now given by

$$A_k^2 = \frac{1}{2\pi} \int_{-\infty}^{\infty} S_{MEG}^k(\omega) d\omega,$$

where $S_{MEG}^k(\omega)$ denotes the k-th entry on the diagonal of $S_{MEG}(\omega)$. In the calculation of source-strengths, we sampled S_{MEG}^k between 0 and 40 Hz with spectral resolution $\Delta\omega = 0.1$ Hz.

Appendix E. Functional correlations

The cross-correlation function $\Gamma_{MEG}^{k,l}(\tau)$ between the MEG signals at regions k and l at lag τ is given by the normalized inverse Fourier transform of the cross-spectrum between regions k and l

$$\Gamma_{MEG}^{k,l}(\tau) = \frac{1}{A_k A_l} \int_{-\infty}^{\infty} S_{MEG}^{k,l}(\omega) e^{i\tau\omega} d\omega,$$

where $S_{MEG}^{k,l}(\omega)$ denotes the (k, l)-th entry of $S_{MEG}(\omega)$. In particular, the functional connectivity between region k and l as characterized by the correlation coefficient between the corresponding MEG signals is given by $\Gamma_{MEG}^{k,l}(0)$. In the calculation of the correlation coefficients, we sampled S_{MEG}^k with spectral resolution

$$\Delta\omega = \frac{2\pi}{4(2N+1)10^{-3}},$$

Hz, which corresponds to a temporal solution of $\Gamma_{MEG}^{k,l}$ of

$$\Delta t = 2\pi / \Delta\omega(2N+1),$$

ms. Setting $N = 200$, this gives $\Delta t = 4$ ms and a maximal observable delay of ± 800 ms.

References

Baar, E., Schürmann, M., Baar-Eroglu, C., Karaka, S., 1997. Alpha oscillations in brain functioning: an integrative theory. Int. J. Psychophysiol. 26 (1-3), 5–29 (June).

Baillet, S., Garnero, L., Marin, G., Hugonin, J.-P., 1999. Combined MEG and EEG source imaging by minimization of mutual information. IEEE Trans. Biomed. Eng. 46 (5).

Behrens, T.E.J., Woolrich, M.W., Smith, S.M., Boulby, P.A., Barker, G.J., Sillery, E.L., Sheehan, K., Ciccarelli, O., Thompson, A.J., Brady, J.M., Matthews, P.M., 2003a. Non-invasive mapping of connections between human thalamus and cortex using diffusion imaging. Nature 6 (7).

Behrens, T.E.J., Woolrich, M.W., Jenkinson, M., Nunes, R.G., Clare, S., Matthews, P.M., Brady, J.M., Smith, S.M., 2003b. Characterization and propagation of uncertainty in diffusion-weighted MR imaging. Magn. Reson. Med. 50, 1077–1088.

Behrens, T.E.J., Berg, H.J., Jbabdi, S., Rushworth, M.F.S., Woolrich, M.W., 2007. Probabilistic diffusion tractography with multiple fibre orientations: what can we gain? Neuroimage 34, 144–155.

Berger, H., 1875. Uber das elektrenkephalogramm des menschen. Eur. Arch. Psychiatry Clin. Neurosci. 278, 1929.

Bojak, I., Liley, D., 2005. Modeling the effects of anesthesia on the electroencephalogram. Phys. Rev. E 71 (4), 1–22 (April).

Bojak, I., Oostendorp, T.F., Reid, A.T., Kötter, R., 2010. Connecting mean field models of neural activity to EEG and fMRI data. Brain Topogr. 23, 139–149.

Bojak, I., Oostendorp, T.F., Reid, A.T., Kötter, R., 2011. Towards a model-based integration of co-registered electroencephalography / functional magnetic resonance imaging data with realistic neural population meshes. Philos. Transact. A Math. Phys. Eng. Sci. 369, 3785–3801.

Bollimunta, A., Chen, Y., Schroeder, C.E., Ding, M., 2008. Neuronal mechanisms of cortical alpha oscillations in awake-behaving macaques. J. Neurosci. 28 (40), 9976–9988 (October).

Bollimunta, A., Mo, J., Schroeder, C.E., Ding, M., 2011. Neuronal mechanisms and attentional modulation of corticothalamic α oscillations. J. Neurosci. 31 (13), 4935–4943 (March).

Breakspear, M., Roberts, J.A., Terry, J.R., Rodrigues, S., Mahant, N., Robinson, P.A., 2006. A unifying explanation of primary generalized seizures through nonlinear brain modeling and bifurcation analysis. Cereb. Cortex 16 (9), 1296–1313 (September).

Cabral, J., Hugues, E., Sporns, O., Deco, G., 2011. Role of local network oscillations in resting-state functional connectivity. Neuroimage 57, 130–139.

Capilla, A., Schoffelen, J.-M., Paterson, G., Thut, G., Gross, J., 2012. Dissociated α-band modulations in the dorsal and ventral visual pathways in visuospatial attention and perception. Cereb. Cortex 1–12.

Ciulla, C., Takeda, T., Hiroshi, E., 1999. MEG characterization of spontaneous alpha rhythm in the human. Brain 11 (3), 211–222.

Collins, D., Neelin, P., Peters, T., Evans, A.C., 1994. Automatic 3D intersubject registration of MR volumetric data in standardized Talairach space. J. Comput. Assist. Tomogr. 18, 192–205.

Dale, A.M., Sereno, M.I., 1993. Improved localization of cortical activity by combining EEG and MEG with MRI cortical surface reconstruction: a linear approach. J. Cogn. Neurosci. 5 (2), 162–176.

David, O., Kiebel, S.J., Harrison, L.M., Mattout, J., Kilner, J.M., Friston, K.J., 2006. Dynamic causal modeling of evoked responses in EEG and MEG. Neuroimage 30 (4), 1255–1272 (May).

Deco, G., Jirsa, V.K., 2012. Ongoing cortical activity at rest: criticality, multistability, and ghost attractors. J. Neurosci. 32 (10), 3366–3375.

Deco, Gustavo, Jirsa, Viktor K., Robinson, Peter A., Breakspear, Michael, Friston, Karl, 2008. The dynamic brain: from spiking neurons to neural the dynamic brain: from spiking neurons to neural masses and cortical fields. PLoS Comput. Biol. 4 (8).

Deco, G., Jirsa, V., Mcintosh, A.R., Sporns, O., Kotter, R., 2009. Key role of coupling, delay, and noise in resting brain fluctuations. Proc. Natl. Acad. Sci. U. S. A. 106 (25), 10302–10307.

Deco, G., Jirsa, V.K., Mcintosh, A.R., 2011. Emerging concepts for the dynamical organization of resting-state activity in the brain. Nat. Rev. Neurosci. 12, 43–56.

Deco, G., Ponce-Alvarez, A., Mantini, D., Romani, G.L., Hagmann, P., Corbetta, M., 2013. Resting-state functional connectivity emerges from structurally and dynamically shaped slow linear fluctuations. J. Neurosci. 33 (27), 11239–11252.

Feige, B., Scheffler, K., Esposito, F., Salle, F.D., Seifritz, E., Scheffler, K., Di, F., 2005. Cortical and subcortical correlates of electroencephalographic alpha rhythm modulation. J. Neurophysiol. 93, 2864–2872.

Freeman, W.J., 2004. Mass Action in the Nervous System.

Freeman, W.J., Barrie, J.M., Wang, X.-J., 2000. Analysis of spatial patterns of phase in neocortical gamma EEGs in rabbit. J. Neurophysiol. 84, 1266–1278.

Ghosh, A., Rho, Y., McIntosh, A.R., Kotter, R., Jirsa, V.K., 2008. Noise during rest enables the exploration of the brain's dynamic repertoire. PLoS Comput. Biol. 4 (10).

Goldman, R.I., Stern, J.M., Engel, J., Cohen, M.S., 2002. Simultaneous EEG and fMRI of the alpha rhythm. Neuroreport 13 (18), 2487–2492 (December).

Hamalainen, M., Hari, R., Ilmoniemi, R.J., Knuutila, J., Lounasmaa, O.V., 1993. Magnetoencephalographytheory, instrumentation, and applications to noninvasive studies of the working human brain. Rev. Mod. Phys. 65.

Hari, R., Salmelin, R., 1997. Human cortical oscillations: a neuromagnetic view through the skull. Trends Neurosci. 20 (1), 44–49.

Hindriks, R., van Putten, M.J.A.M., 2012. Meanfield modeling of propofol-induced changes in spontaneous EEG rhythms. Neuroimage 60, 2323–2334 (February).

Hindriks, R., Bijma, F., van Dijk, B.W., van der Werf, Y.D., van Someren, E.J.W., van der Vaart, A.W., 2011. Dynamics underlying spontaneous human alpha oscillations: a data-driven approach. Neuroimage 57 (2), 440–451 (July).
Hindriks, R., van Putten, M.J.A.M., Deco, G., 2014. Intra-cortical propagation of EEG alpha oscillations. Neuroimage 103, 444–453.
Honey, C.J., Sporns, O., Cammoun, L., Gigandet, X., Thiran, J.P., Meuli, R., Hagmann, P., 2009. Predicting human resting-state functional connectivity. Proc. Natl. Acad. Sci. U. S. A. 106 (6), 1–6.
Huang, M.X., Mosher, J.C., Leahy, R.M., 1999. A sensor-weighted overlapping-sphere head model and exhaustive head model comparison for MEG. Phys. Med. Biol. 44, 423–440.
Hughes, S.W., Lörincz, M., Cope, D.W., Blethyn, K.L., Kékesi, K.A., Parri, H.R., Juhász, G., Crunelli, V., 2004. Synchronized oscillations at alpha and theta frequencies in the lateral geniculate nucleus. Neuron 42 (2), 253–268 (April).
Hutt, A., Longtin, A., 2010. Effects of the anesthetic agent propofol on neural populations. Cogn. Neurodyn. 4, 37–59 (September).
Hyvarinen, A., 1999. Fast and robust fixed-point algorithms for independent component analysis. IEEE Trans. Neural Netw. 10 (3), 626–634.
Jansen, B.H., Rit, V.G., 1995. Electroencephalogram and visual evoked potential generation in a mathematical model of coupled cortical columns. Biol. Cybern. 366, 357–366.
Jenkinson, M., Bannister, P., Brady, M., Smith, S., 2002. Improved optimization for the robust and accurate linear registration and motion correction of brain images. Neuroimage 17, 825–841.
Jensen, O., Gelfand, J., Kounios, J., Lisman, J., 2002. Oscillations in the alpha band (9–12 Hz) increase with memory load during retention in a short-term memory task. Cereb. Cortex 12 (8), 877–882 (August).
Jensen, O., Mazaheri, A., Box, O., 2010. Shaping functional architecture by oscillatory alpha activity: gating by inhibition. Front. Hum. Neurosci. 4 (186), 1–8.
Jirsa, V.K., Kelso, J.A.S., 2000. Spatiotemporal pattern formation in neural systems with heterogeneous connection topologies. Phys. Rev. E 62 (6), 8462–8465.
Jirsa, V.K., Jantzen, K.J., Fuchs, A., Kelso, J.A.S., 2002. Spatiotemporal forward solution of the EEG and MEG using network modeling. IEEE Trans. Med. Imaging 21 (5), 493–504.
Jokisch, D., Jensen, O., 2007. Modulation of gamma and alpha activity during a working memory task engaging the dorsal or ventral stream. J. Neurosci. 27 (12), 3244–3251.
Karameh, F.N., Dahleh, M.A., Brown, E.N., Massaquoi, S.G., 2006. Modeling the contribution of lamina 5 neuronal and network dynamics to low frequency EEG phenomena. Biol. Cybern. 95 (4), 289–310 (October).
Kelly, S.P., Lalor, E.C., Reilly, R.B., Foxe, J.J., Simon, P., Lalor, E.C., Reilly, R.B., 2006. Increases in alpha oscillatory power reflect an active retinotopic mechanism for distracter suppression during sustained visuospatial attention. J. Neurophysiol. 95, 3844–3851.
Klimesch, W., 1999. EEG alpha and theta oscillations reflect cognitive and memory performance: a review and analysis. Brain Res. Brain Res. Rev. 29 (2–3), 169–195 (April).
Klimesch, W., Doppelmayr, M., Russegger, H., Pachinger, T., Schwaiger, J., 1998. Induced alpha band power changes in the human EEG and attention. Neurosci. Lett. 244 (2), 73–76 (March).
Liley, D.T.J., Cadusch, P.J., 2002. A spatially continuous mean field theory of electrocortical activity. Netw. Comput. Neural Syst. 13 (1), 67–113 (February).
Liley, D.T.J., Cadusch, P.J., Wright, J.J., 1999. A continuum theory of electro-cortical activity. Neurocomputing 26–27, 795–800 (June).
Lopes Da Silva, F.H., 2013. EEG and MEG: relevance to neuroscience. Neuron 80 (5), 1112–1128.
Lopes Da Silva, F.H., Storm van Leeuwen, W., 1977. The cortical source of the alpha rhythm. Neurosci. Lett. 6 (2–3), 237–241.
Lopes da Silva, F.H., van Lierop, T.H.M.T., Schrijer, C.F., Storm van Leeuwen, W., 1973. Essential differences between alpha rhythms and barbiturate spindles: spectra and thalamo-cortical coherences. Electroencephalogr. Clin. Neurophysiol. 35, 641–645.
Lopes da Silva, F.H., Hoeks, A., Smits, H., Zetterberg, L.H., 1974. Model of brain rhythmic activity. Kybernetik 15, 27–37.
Lopes Da Silva, F.H., Vos, J.E., Mooibroek, J., van Rotterdam, A., 1980. Relative contributions of intracortial and thalamo-cortical processes in the generation of alpha rhythms, revealed by partial coherence analysis. Electroencephalography 50, 449–456.
Mantini, D., Penna, S.D., Marzetti, L., de Pasquale, F., Pizzella, V., Corbetta, M., Romani, G.L., 2011. A signal-processing pipeline for magnetoencephalography resting-state networks. Brain Connect. 1 (1).
Mattout, J., Henson, R.N., Friston, K.J., 2007. Canonical source reconstruction for MEG. Comput. Intell. Neurosci. 67613.
Moosmann, M., Ritter, P., Krastel, I., Brink, A., Thees, S., Blankenburg, F., Taskin, B., Obrig, H., Villringer, A., 2003. Correlates of alpha rhythm in functional magnetic resonance imaging and near infrared spectroscopy. Neuroimage 20, 145–158.
Moran, R.J., Kiebel, S.J., Stephan, K.E., Reilly, R.B., Daunizeau, J., Friston, K.J., 2007. A neural mass model of spectral responses in electrophysiology. Neuroimage 37 (3), 706–720 (September).
Nolte, G., 2003. The magnetic lead field theorem in the quasi-static approximation and its use for magnetoencephalography forward calculation in realistic volume conductors. Phys. Med. Biol. 48, 3637–3652.
Nunez, P.L., 1974. The brain wave equation: a model for the EEG. Math. Biosci. 21, 279–297.
Nunez, P.L., Srinivasan, R., 2006. Electric Fields of the Brain. The Neurophysics of EEG.
Nunez, P.L., Wingeier, B.M., Silberstein, R.B., 2001. Spatial-temporal structures of human alpha rhythms: theory, microcurrent sources, multiscale measurements, and global binding of local networks. Hum. Brain Mapp. 164, 125–164.
Rennie, C.J., Wright, J.J., Robinson, P.A., 2000. Mechanisms of cortical electrical activity and emergence of gamma rhythm. J. Theor. Biol. 205 (1), 17–35 (July).
Rennie, C.J., Robinson, P.A., Wright, J.J., 2002. Unified neurophysical model of EEG spectra and evoked potentials. Biol. Cybern. 86 (6), 457–471 (June).
Rihs, T.A., Michel, C.M., Thut, G., 2007. Mechanisms of selective inhibition in visual spatial attention are indexed by a -band EEG synchronization. Eur. J. Neurosci. 25, 603–610.
Robinson, P.A., Rennie, C.J., Wright, J.J., 1997. Propagation and stability of waves of electrical activity in the cerebral cortex. Phys. Rev. E 56 (1), 826 (July).
Robinson, P.A., Rennie, C.J., Wright, J.J., Bahramali, H., Gordon, E., Rowe, D.L., 2001. Prediction of electroencephalographic spectra from neurophysiology. Phys. Rev. E 63 (2), 19–33 (January).
Robinson, P.A., Rennie, C.J., Rowe, D.L., 2002. Dynamics of large-scale brain activity in normal arousal states and epileptic seizures. Phys. Rev. E 65 (4), 1–9 (April).
Romei, V., Brodbeck, V., Michel, C., Amedi, A., Pascual-Leone, A., Thut, G., 2008. Spontaneous fluctuations in posterior alpha-band EEG activity reflect variability in excitability of human visual areas. Cereb. Cortex 18 (2010–2018).
Saalmann, Y.B., Pinsk, M.A., Wang, L., Li, X., Kastner, S., 2012. The pulvinar regulates information transmission between cortical areas based on attentional demands. Science 337, 753–756.
Salmelin, R., Hari, R., 1994. Characterization of spontaneous MEG rhythms in healthy adults. Electroencephalogr. Clin. Neurophysiol. 91, 237–248.
Shipp, S., 2003. The functional logic of cortico-pulvinar connections. Philos. Trans. R. Soc. Lond. B Biol. Sci. 358, 1605–1624.
Silva, L.R., Amitai, Y., Connors, B.W., 1991. Intrinsic oscillations of neocortex generated by layer 5 pyramidal neurons. Science 251, 432–435.
Snyder, A.C., Foxe, J.J., 2010. Anticipatory attentional suppression of visual features indexed by oscillatory alpha-band power increases: a high-density electrical mapping study. J. Neurosci. 30 (11), 4024–4032.
Spaak, E., Bonnefond, M., Maier, A., Leopold, D.A., Jensen, O., 2012. Layer-specific entrainment of gamma-band neural activity by the alpha rhythm in monkey visual cortex. Curr. Biol. 22, 2313–2318.
Stam, C.J., Pijn, J.P.M., Suffczynski, P., Lopes da Silva, F.H., 1999. Dynamics of the human alpha rhythm: evidence for non-linearity? Clin. Neurophysiol. 110 (10), 1801–1813 (October).
Steyn-Ross, D.A., Steyn-Ross, M.L., Sleigh, J.W., Wilson, M.T., Gillies, I.P., Wright, J.J., 2005. The sleep cycle modelled as a cortical phase transition. J. Biol. Phys. 31 (3–4), 547–569 (December).
Suffczynski, P., Kalitzin, S., Lopes Da Silva, F.H., 2004. Dynamics of non-convulsive epileptic phenomena modeled by a bistable neuronal network. Neuroscience 126 (2), 467–484 (January).
Taula, S., Simola, J., Kajola, M., 2005. Applications of the signal space separation method. IEEE Trans. Image Process. 53 (9), 3359–3372.
Tzourio-Mazoyer, N., Landeau, B., Papathanassiou, D., Crivello, F., Etard, O., Delcroix, N., Mazoyer, B., Joliot, M., 2002. Automated anatomical labeling of activations in SPM using a macroscopic anatomical parcellation of the MNI MRI single-subject Brain. Neuroimage 289, 273–289.
Van Harteveld, T.J., Cabral, J., Deco, G., Moller, A., Green, A.L., Aziz, T.Z., Kringelbach, A.L., 2014. Neural plasticity in human brain connectivity: the effects of long term deep brain stimulation of the subthalamic nucleus in Parkinson's disease. PLoS One 9 (e86496).
Wilson, H.R., Cowan, J.D., 1973. A mathematical theory of the functional dynamics of cortical and thalamic nervous tissue. Kybernetik 13 (2), 55–80 (September).
Woolrich, M., Hunt, L., Groves, A., Barnes, G., 2011. MEG beamforming using Bayesian PCA for adaptive data covariance matrix regularization. Neuroimage 57 (4), 1466–1479.
Wright, J.J., Liley, D.T., 1995. Simulation of electrocortical waves. Biol. Cybern. 72 (4), 347–356 (January).
Yamagishi, N., Goda, N., Callan, D.E., Anderson, S.J., Kawato, M., 2005. Attentional shifts towards an expected visual target alter the level of alpha-band oscillatory activity in the human calcarine cortex. Cogn. Brain Res. 25, 799–809.